Article

Finned-tube-integrated modular thermal storage systems for HVAC load modulation in buildings

Kishore et al. investigate a finned-tube-integrated modular thermal energy storage system, which is simple in design, easy to manufacture, and cost-effective due to standard components. The comprehensive study presented here may provide the required guidance and tools to building researchers and engineers for developing the next-generation thermal storage systems.

Ravi Anant Kishore, Allison Mahvi, Ayushman Singh, Jason Woods

ravi.kishore@nrel.gov (R.A.K.)
jason.woods@nrel.gov (J.W.)

Highlights

Shell-and-tube-type finned thermal storage system for buildings

More metallic fins are not always beneficial due to decrease in TES energy density

Less fins provide higher specific energy and energy density at low C rates
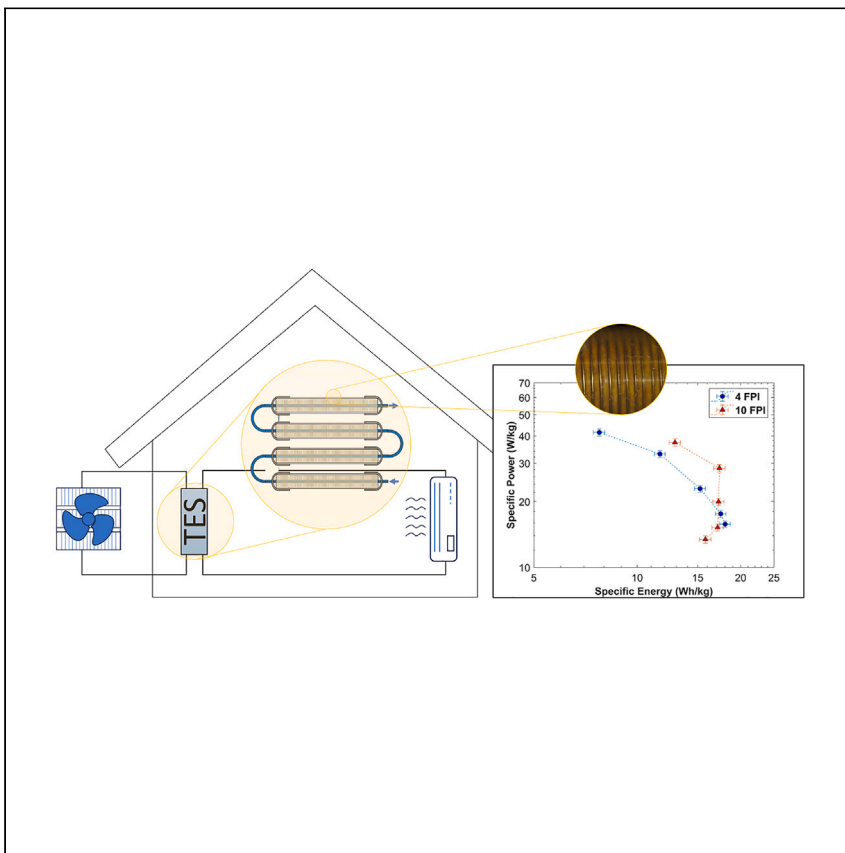
More fins are beneficial at high C rates

Article

Finned-tube-integrated modular thermal storage systems for HVAC load modulation in buildings

Ravi Anant Kishore,[1,4,*] Allison Mahvi,[1,2] Ayushman Singh,[1,3] and Jason Woods[1,*]

SUMMARY

While there is considerable focus on latent-based thermal energy storage (TES) systems, the low thermal conductivity of phase change materials (PCMs) remains a critical concern. Many approaches to enhance PCM conductivity either require complicated synthesis processes or are cost prohibitive. In this study, we investigate finned-tube modular TES systems, which are simple in design, easy to manufacture, and cost-effective due to their standard materials and components. The study includes detailed modeling and experimentation of two devices containing similar amounts of PCM but different fin spacings. The study reveals that having more fins does not necessarily increase the TES thermal performance because the reduction in the PCM volume fraction can reduce the TES volumetric and specific energy densities. We find that larger fin spacings provide a higher specific energy for lower C rates (<1C), while smaller fin spacings provide a higher specific energy for higher C rates (>1C).

INTRODUCTION

Thermal energy storage (TES) systems can provide energy savings and load flexibility for a wide range of applications, such as solar energy conversion,[1,2] electronics cooling,[3,4] and thermal management in buildings.[5–7] A TES system stores surplus heat and releases it at a later time, thereby reducing the mismatch between demand and supply of energy. This method has been proven to enhance the performance and reliability of energy conversion systems, including heat pumps, by enhancing their coefficient of performance and energy distribution networks by reducing waste heat.[8–10] TES systems are usually based on sensibly heating or cooling a material with a high specific heat, or exploiting a phase change process such as melting, solidification, or vaporization to store thermal energy (termed latent TES).[10] Due to the large amount of latent heat that is stored or released during phase change processes, phase change materials (PCMs) are typically more energy dense than the sensible materials.[8,11,12] In addition, PCMs change phase at nearly constant temperature, hence mitigating the considerable temperature increase and making them easier to integrate into thermal systems.

PCM-based TES systems have been widely reported in the literature for variety of applications including concentrated solar power,[13] energy conversion,[14] cold storage,[15,16] and thermal management in buildings.[17,18] Heating and cooling buildings is one important application of thermal storage systems. Recent efforts have focused on integrating PCMs into building envelopes,[19,20] heat pumps,[21] and water heaters.[21] The building sector accounts for about 40% of global energy consumption, and nearly 50% of this energy is used for heating, ventilation, and air conditioning (HVAC).[22,23] In addition, the building sector is responsible for nearly 39% of

[1]National Renewable Energy Laboratory, 15013 Denver West Pkwy, Golden, CO 80401, USA

[2]University of Wisconsin-Madison, Madison, WI 53706, USA

[3]State University of New York at Binghamton, Binghamton, NY 13902, USA

[4]Lead contact

*Correspondence: ravi.kishore@nrel.gov (R.A.K.), jason.woods@nrel.gov (J.W.)

https://doi.org/10.1016/j.xcrp.2023.101704

global carbon dioxide (CO_2) emissions.[24,25] With the increasing penetration of renewable energy in the total energy generation mix, matching the variations in energy supply with demand in a sustainable and efficient manner is a major challenge. To this end, latent heat storage is being explored for various applications in buildings.[26,27] The choice of PCM used for building applications is determined based on its thermophysical properties, such as transition temperature, latent heat of fusion, and thermal conductivity, and other practical considerations such as supercooling, corrosiveness, toxicity, and flammability.[28,29]

The latent heat of the PCMs dictates the total energy storage capacity per unit volume or mass, in other words the specific energy and energy density, of the TES system. This is important for building applications, which often are space and weight constrained. Due to recent advancements in material development, many organic and inorganic PCMs with energy density ~200 kJ kg^{-1} are commercially available. However, a major shortcoming of most PCMs is the low intrinsic thermal conductivity (0.2–1.0 W m^{-1} K^{-1}),[29] which restricts the heat transfer rate in/out of the TES, thereby limiting their power and energy availability under the desired response time. More specifically, due to low thermal conductivity, the usable energy density of TES reduces at higher charge or discharge rates.[30]

Various techniques to enhance the thermal conductance of TES systems have been proposed that integrate high thermal conductivity materials into a PCM composite. Thermally conductive enhancer/filler materials such as micro/macroscale metal fins, foams, honeycombs, and three-dimensional (3D)-printed lattices and scaffolds have been recommended as the potential solutions.[31–33] In recent years, nanoscale additives, such as graphite nanoparticles, graphene nanoplatelets, graphite foams, and other carbon-based high thermal conductivity fillers have also been successfully developed and investigated.[34,35] In these studies, the high thermal conductivity filler increases the effective thermal conductivity of PCM composite by over an order of magnitude depending on the filler's thermal conductivity; however, this advantage comes with the penalty of reducing the total volume fraction of the PCM. In addition, while various techniques such as the carbon-based filler with a very high intrinsic thermal conductivity provides better trade-off between TES energy density and power, these techniques involve complicated synthesis processes, which are often cost-prohibitive to implement for practical applications.

Prior studies in the literature have evaluated various thermally conductive materials, geometries, and methods to optimize the energy and power densities of PCM-based TES systems. Various design configurations are proposed in the literature; however, the primary goal remains the same which is to maximize the TES charge/discharge energy capacity under the desired response time, while minimizing the materials used. Among various conductive filler options, metallic fins are promising because of their simple design, low manufacturing cost, and ease of use in thermal storage heat exchangers. The most common finned-based TES device typically includes a larger tube (shell) and one (central) or more (distributed) smaller tubes.[36] The PCM can be filled either in the shell or in the tubes and a fluid is passed to charge and discharge the PCM.[37] Metallic fins are typically attached to the outer surface of the tubes, either in a radial or longitudinal arrangement. While it is difficult to cover the entire literature, here we summarize some of the important reports relevant to this study.

- Deng et al.[38] compared the thermal performance of various TES comprising no fins, straight longitudinal fins, angled longitudinal fins, and lower and upper

longitudinal fins using an experimentally validated 2D numerical model. The TES performance was described based on heat storage capacity and total melting time. It was noted that there exists an optimal number of fins, which equals six longitudinal fins, where the optimum arrangement changes from the lower fin configuration to the angled fin configuration.

- Triscari et al.[18] compared the performance of radial and longitudinal fins in shell and tube heat exchangers using a finite element model. The design variables used in the optimization were pitch of the tube bundle, fin dimension, and specific number of fins, while the optimization target was to achieve 7 kW thermal power using the least amount of material by mass. It was found that the optimized longitudinal fin design used less material to achieve the same thermal power as the optimized radial fin design. The final longitudinal design met the target performance with a power density of 57.9 W/kg, whereas the radial design only reached a power density of 20.8 W/kg.

- One key demerit of the conventional longitudinal fins is that the fin spacing increases as the radius of the fins increases, which leads to low local thermal conductance and temperature inconsistency near the circumference. To manage this issue, Zhang et al.[39] recommended a bionic design using Y- or tree-shaped fins that resulted in a faster solidification rate, higher energy discharge rate, and better temperature uniformity than the conventional fins. The complete solidification time of the tree-fins unit decreased by 66.2%, but the melting time reduced only by 4.4%. The smaller reduction in the melting time was attributed to the greater restriction of natural convection by the tree-shaped fins than the radial fins.

- Yang et al.[40] experimentally studied and visualized the melting and solidification process in a 3D-printed TES containing aluminum fins in the radial configuration charged with a PCM with a transition temperature of 35°C. The theoretical and experimental energy balance were found to be within ±9%.

- Gil et al.[41] studied the effect of adding fins/baffles radially in a bulk TES tank with tube bundles using hydroquinone as the PCM. The effective thermal conductance with fins was enhanced by 4.1% at higher thermal power and 25.8% at lower thermal power. They found that, at low thermal power, the melt fraction increased faster in the fin cases; however, at high thermal power, the melting behavior was same as the no-fins case. The fluid flow regime at high thermal power changed from laminar to intermediate/turbulent, thus enhancement due to fins became less important than the enhancement in the increased convective heat transfer coefficient.

- Another study on radially oriented fins was performed by Rahimi et al.[42] They conducted experiments on finned-tube storage unit with heat transfer fluid circulating in the tubes using paraffin RT 35 as PCM and compared the results with a finless heat exchanger. The varied parameters in the study were the inlet heat transfer fluid temperature and flow rate. At a fixed flow rate of 0.6 L/min, the melting time was reduced by almost 50% with fins at 50°C, 60°C, and 70°C inlet temperatures. At a fixed inlet temperature of 60°C, the melting time reduction with the fins was almost 50% at 0.4 and 0.6 L/min flow rate; however, at a higher flow rate of 1.6 L/min the reduction in the melting time was just 20%. Also, for the finless heat exchanger, the melting time was reduced by 52% when the flow regime was altered from laminar to turbulent.

We can note that both longitudinal and radial fins have been proposed in the literature. Longitudinal finned tubes typically require less material; however, this results in a radially decreasing effective thermal conductance. Some innovative fin designs such as tree- or Y-shaped fins have been recommended to tackle this issue but these

kinds of designs are challenging to procure and scale cost-effectively. Therefore, in this study, we have used the radial configuration because of its simplicity, availability, and scalability.[43] In addition, prior work recommends that the shell should contain PCM and the fluid should flow through the tubes as it reduces the required PCM thickness and lowers heat loss from the fluid to the ambient.[44] In this study, we have chosen the recommended configuration, henceforth referred to as shell-and-tube TES, with PCM in the shell and fluid in the tube.

While various prior publications have reported shell-and-tube-type TES systems, none evaluate performance using the Ragone framework. The Ragone framework not only quantifies TES performance in terms of its energy storage capacity and power but also collectively compares the energy and power densities. This is crucial for PCM-based thermal storage, which contains thermal conductivity fillers as well as other auxiliary components like thermal fluid, insulations, etc., that can considerably increase the mass and volume of the systems. The primary goal of this study is to design, develop, and test a TES system that can provide cooling for at least 1 h. While the full-scale TES for a typical residential home requires an energy storage capacity of about 3–5 tonh (10.6–17.6 kWh), in this study we have investigated a scaled-down TES of about 330 Wh capacity. In addition, this study is limited to TES characterization only; its integration with an HVAC system is beyond our scope. More specifically, in this work, we experimentally evaluate a shell-and-tube-type TES device and determine if simplified effective medium models can accurately predict heat transfer through metallic fin PCM composites. In our experimental work, we evaluate the performance of two different 330 Wh TES devices with different fin pitches. The results include rate capability curves and Ragone plots, showing the impact of fin density on performance at different power levels. With these data, we then evaluate the use of finite difference models with effective medium properties to predict the performance of finned shell-and-tube TES heat exchangers.

RESULTS

TES design concept

The shell-and-tube TES device was initially designed using the finite difference model described in a subsequent section. In this effort, we evaluated the device performance for a range of design variables (fin pitch, fin length, tube diameter, etc.) and selected the design with the largest energy density for a 1-h discharge. In this analysis we found that larger fin spacings (∼6 mm) were preferable, but prior work suggests that effective medium theory, which was used in the finite difference model, may not apply.[45] To probe this, we built two test sections with different fin pitches and evaluated their performance. These devices are described in more detail in the subsequent sections.

The purpose of this study was to specifically look at the PCM composite structure to understand if our model assumptions were accurate. The final test section was not one of these optimized designs, but rather commercial off-the-shelf finned tubes that most closely matched the fin length and spacing from our initial optimization results. We could not find commercially available heat exchangers that matched our design criteria, so we prioritized the PCM composite properties over other parameters. One example of this was the selected tube diameter. In both test sections, the tube diameter was too large, which results in laminar flow of the heat transfer fluid and a relatively large convective thermal resistance. To get around this problem, we inserted a solid rod inside the tubes to increase the flow velocity. This allowed for better performance but is an obvious waste of space inside the device.
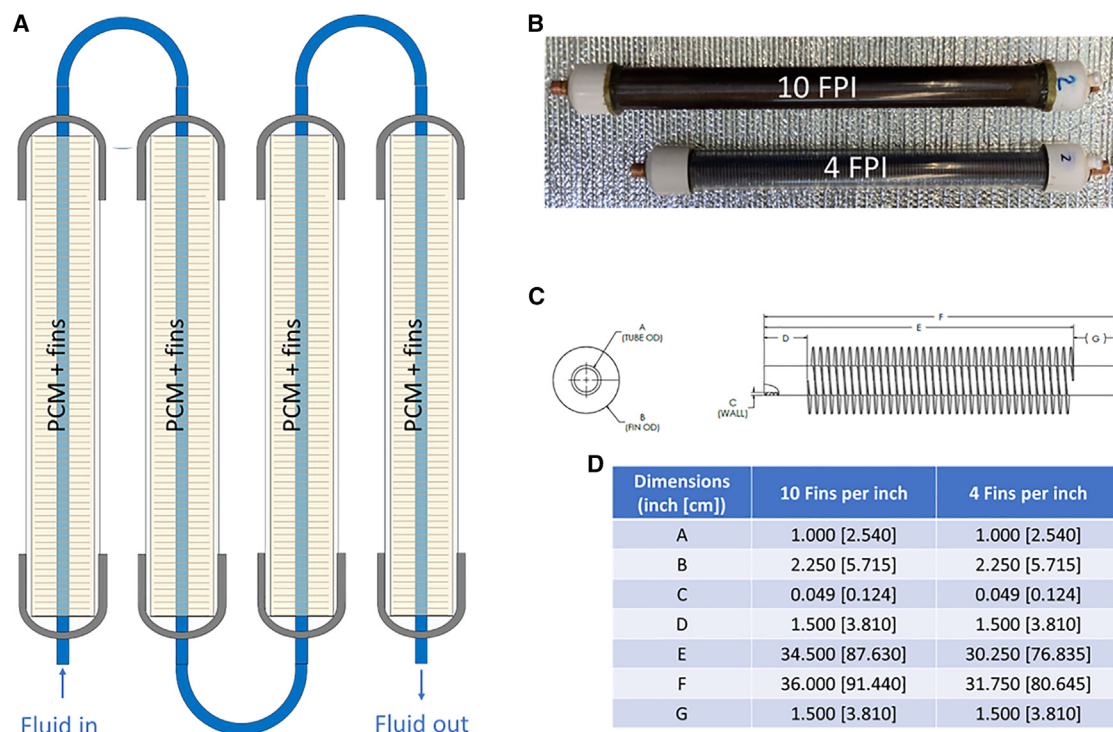
Figure 1. Shell-and-tube TES system
(A) TES layout, (B) 4 and 10 FPI fins with PureTemp 4 PCM, (C) fins configuration, and (D) key geometric dimensions.

Future designs would likely need to be made with custom-manufacturing approaches to reach their full potential.

Figure 1 depicts the shell-and-tube TES systems investigated in this study. We considered two different types of finned tubes having similar dimensions but different fin spacings: 4 and 10 fins per inch (FPI). The length of the 10 FPI TES is larger than that of the 4 FPI TES. This was needed to allow for the same amount of PCM in each shell, thereby ensuring nearly the same energy storage capacity of the two TES systems. The PCM used in this study is PureTemp 4, which has a melting point of 5°C and latent heat storage capacity of 187 kJ kg^{-1}. The heat transfer fluid employed here is a propylene glycol-water mixture (25% v/v) with a freezing point of around −10°C.

Experimental characterization

The schematic shown in Figure 2 illustrates the test setup used for the experiments. The test rig includes a chiller, a variable-speed diaphragm pump, and a heater with a feedback loop to manage the set-point temperature. There are three thermocouples each at the inlet and outlet of the TES, a flowmeter with a feedback loop to manage the preset flowrate, and a few quarter-turn flow valves to select the appropriate flow path for charge and discharge modes.

Charging mode (freezing)

For all the experiments described in this study, the devices were charged at a fixed circulating bath temperature. Figure 3A illustrates the fluid inlet and outlet temperature when the TES is charged. The chiller bath temperature was maintained at −6°C initially, and then later at 0°C. The lower bath temperature of −6°C increases the charging rate of the TES, while 0°C is the target isothermal state of the TES before the discharge process begins.
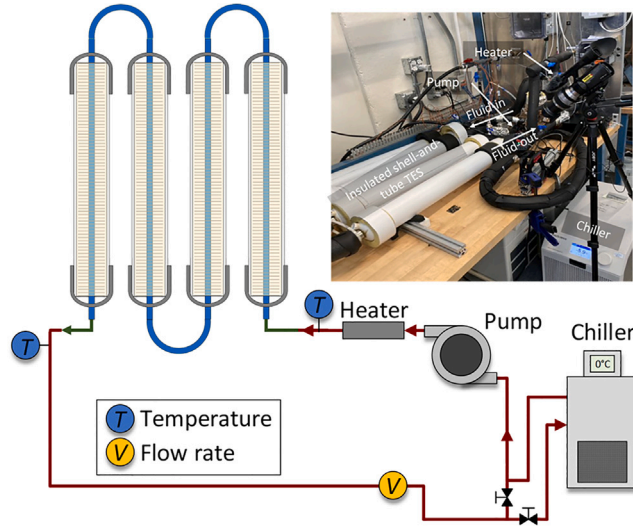
Figure 2. Schematic illustrating the experimental setup, key components, and operation
The picture in the inset shows the actual test rig with shell and 10 FPI tube TES under fiberglass insulation.

Discharging mode (melting)
In this work, we discharged the TES in two ways. First, we kept the inlet temperature into the TES device constant by maintaining the chiller bath temperature at 10°C. Figure 3B illustrates the thermal fluid inlet and outlet temperature when the TES is discharged at a constant inlet temperature. The second discharge method maintained a constant heat transfer rate or constant discharge power throughout the experiment, where a constant temperature difference between the fluid inlet and outlet was maintained using the external heater and a feedback loop. For all constant power experiments, the fluid temperature difference was maintained at 4°C while the flow rate was varied to achieve the desired C rate (discharge power over a desired time period). C rate is defined as the desired heat transfer rate (W) divided by the TES maximum discharge capacity (Wh). The flow rate was controlled using the variable speed pump connected to a remotely controlled DC power supply (BK Precision 1687B). We varied the C rate between 2C/3 and 2C (desired discharge time of 90 to 30 min).

The heat transfer rate ($\dot{Q}_{TES}$) between the fluid and the PCM, or the charging/discharging power, can be calculated based on the fluid inlet and outlet temperature.

$$\dot{Q}_{TES} = \dot{m}_f \, C_{p,f}(T_{f,out} - T_{f,in}) \tag{Equation 1}$$

where $\dot{m}_f$ is the fluid mass flow rate, $C_{p,f}$ is the temperature-dependent specific heat capacity of the fluid, and $T_{f,in}$ and $T_{f,out}$ are fluid inlet and outlet temperatures. While we have used temperature-dependent fluid properties in our calculations, the variation in the specific heat over all experiments was less than 2%.

The TES energy storage capacity (E_{TES}) can be calculated by time integrating the heat transfer rate and accounting for the heat gain from the ambient, which can be estimated using the heat transfer rate at steady state when the TES is fully charged/discharged.

$$\begin{aligned} E_{TES} &= M_{TES} \left(\varphi C_{p,s} \Delta T + (1 - \varphi) C_{p,l} \Delta T + L \right) \\ &= \int_{t=0}^{t=\tau} \dot{m}_f \, C_{p,f} \left(T_{f,out} - T_{f,in} \right) dt \pm \int_{t=0}^{t=\tau} \dot{Q}_{gain} \, dt \end{aligned} \tag{Equation 2}$$
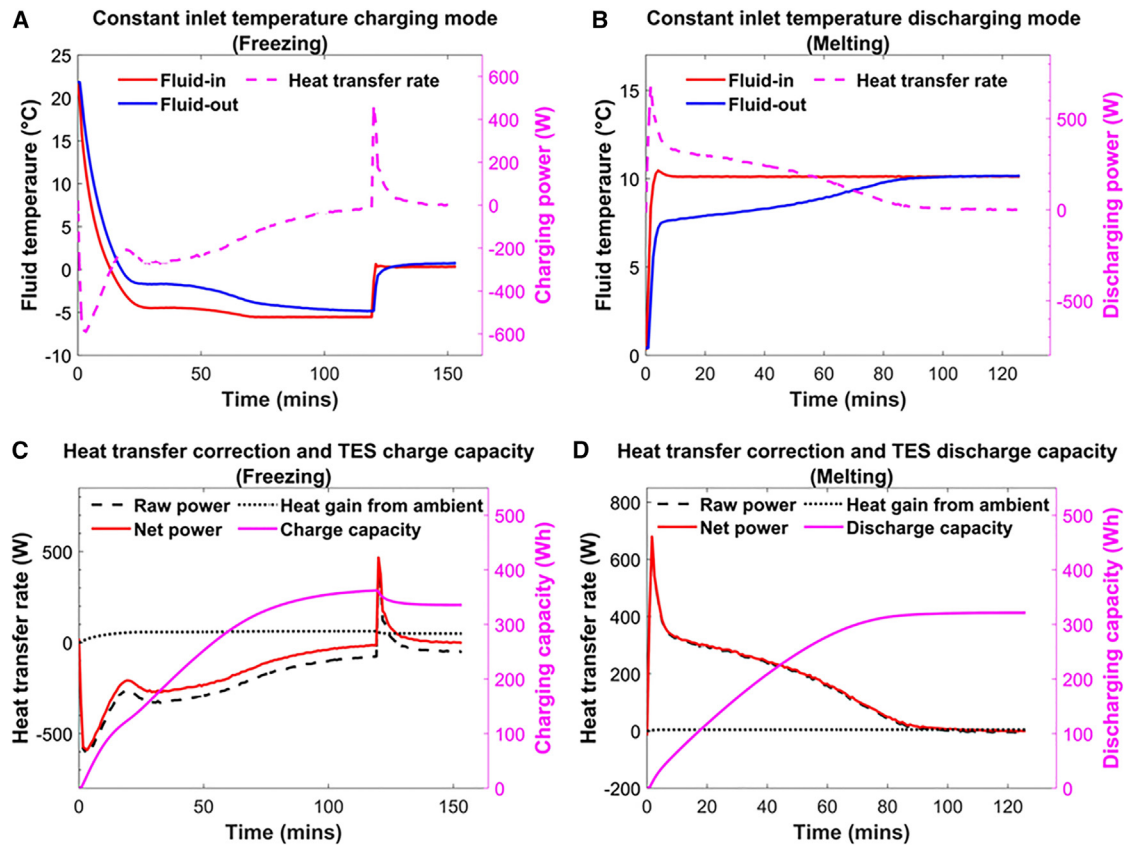
Figure 3. 4 FPI TES charging (freezing) and discharging (melting) modes under constant fluid inlet temperature conditions

The circulating bath temperature was maintained at (A) −6°C for about 2 h and then 0°C for about 30 min during charging and (B) 10°C during discharging. The correction in heat transfer rate due to heat gains from the ambient atmosphere to estimate the net (C) charging and (D) discharging TES energy storage capacity.

where M_{TES} is the TES mass, $(\varphi C_{\text{p,s}} \Delta T + (1 - \varphi) C_{\text{p,l}} \Delta T)$ is the heat capacity associated with the sensible heating/cooling of solid and liquid portion of the TES under temperature change ΔT, φ is the mass fraction of the solid PCM, $C_{\text{p,s}}$ and $C_{\text{p,l}}$ are specific heat of solid and liquid PCM, and L is the latent heat capacity associated with the phase transition.

The heat gain rate from the ambient ($\dot{Q}_{\text{gain}}$) was estimated using:

$$\dot{Q}_{\text{gain}} = \frac{(T_{\text{amb}} - \overline{\overline{T}}_{\text{TES}})}{R_{\text{th}}} \qquad \text{(Equation 3)}$$

where T_{amb} is the ambient temperature, $\overline{T}_{\text{TES}}$ is the average TES temperature, and R_{th} is the thermal resistance between the TES and the ambient atmosphere.

In this work, we calculated the thermal resistance at the fully charged and fully discharged states, where the PCM was at an approximately isothermal state. The thermal resistance R_{th} was estimated using:

$$R_{\text{th}} = \frac{(T_{\text{amb}} - \overline{T}_{\text{f,ss}})}{\dot{Q}_{\text{ss}}} \qquad \text{(Equation 4)}$$

where $\dot{Q}_{\text{ss}}$ is the heat transfer rate in the fully charged or fully discharged states, and $\overline{T}_{\text{f,ss}}$ is the average fluid temperature under these two conditions.

Table 1. TES discharging capacity at constant fluid inlet temperature conditions, where chiller bath temperature was maintained at ~10°C

	4 FPI TES	10 FPI TES
Raw measured energy storage capacity (Wh)	312.1	342.7
Estimated ambient heat gains (Wh)	9.3	30.4
Net measured energy storage capacity (Wh)	321.4	373.1
Calculated storage capacity (Wh)	350.9	347.5

The estimated thermal resistance R_{th} was calculated to be 1.46 ± 0.15 and 0.85 ± 0.05 K/W in fully charged state and 2.37 ± 0.30 and 0.78 ± 0.06 K/W in fully discharged state for 4 FPI and 10 FPI TES, respectively.

Figures 3C and 3D depict the correction in heat transfer rate due to heat gains from the ambient along with the net charging and discharging power and energy storage capacity. Table 1 shows the measured, corrected, and theoretical thermal storage capacity for 4 and 10 FPI TES during the discharging process. The measured energy storage capacity shows the raw data from experiments; the net storage capacity is the measured capacity plus the estimated heat gains from the ambient; and the calculated storage capacity is the theoretical value based on the sensible and latent heat related to the measured mass of the PCM and metallic fins under a temperature change between 0°C and 10°C.

Modeling details

In parallel with the experimental work, we developed a model of the PCM heat exchanger using a finite-difference approach, which we have previously shown to capture the progression of the phase change process in TES heat exchangers.[30] Ultimately, we are interested in developing a computationally inexpensive finned PCM heat exchanger model that can be used for component optimization or system-level analysis. One of the key objectives of this work is to validate the modeling approach for PCM composites with metallic fins. The model geometry is identical to the test section except that the insulated tube bends connecting the finned-tube sections are ignored for simplicity and the PCM outside the finned area is ignored due to its low intrinsic thermal conductivity. As in the experiments, the fluid passed through an annular flow channel with an inner diameter (ID) of 19.1 mm and an outer diameter (OD) of 22.9 mm. The fluid stream was discretized into 40 sub-volumes in the axial direction, and energy balances were imposed that included advection of the fluid (using the upwinding scheme), heat transfer to the surrounding PCM, and internal energy storage. Axial conduction in the fluid was ignored (justified because the minimum Peclet number is 4,185). The heat transfer rate between the fluid nodes and the PCM ($\dot{q}_{f \rightarrow PCM}$) was approximated using the convective fluid resistance and the conductive resistance through the tube wall, where the Rohsenow correlations were used to find the heat transfer coefficients.[46]

The equation describing the fluid temperature change with time is shown in Equation 5, where $c_{p,f}$ is the specific heat capacity of the fluid, $M_{f,i}$ is the mass of the fluid in each node, $\dot{m}_f$ is the mass flow rate of the fluid, T_f is the fluid temperature in each node, and i is the node number in the x direction.

$$\left. \frac{dT_f}{dt} \right|_i = \frac{1}{c_{p,f} M_{f,i}} \left[\dot{m}_f c_{p,f} (T_{f,i-1} - T_{f,i}) - \dot{q}_{f \rightarrow PCM,i} \right] \qquad \text{(Equation 5)}$$

All thermodynamic properties of the fluid are based on a 25% mixture of propylene glycol-water by volume. All fluid properties that changed less than 2% over the

temperature range of interest were held constant, and all other properties were updated in each timestep.

The PCM composite was also discretized, with 20 sub-volumes in the radial direction and 40 sub-volumes in the axial direction. The number of nodes were chosen such that doubling them at the highest discharge rate resulted in a less than 2% change in the calculated specific energy. The heat transfer between adjacent PCM nodes is calculated with a discretized version of Fourier's law, accounting for directional differences in the thermal conductivity of the composite materials. The resulting enthalpy change with time of each PCM node is calculated with a nodal energy balance:

$$
\left.\frac{dh}{dt}\right|_{i,j} = \frac{2\pi}{M_{i,j}} \left[\frac{k_\perp r_j dr}{dx} \left(T_{i-1,j} + T_{i+1,j} - 2T_{i,j}\right) + \frac{k_\parallel dx}{\ln\left(\frac{r_{j+1}}{r_j}\right)} \left(T_{i,j+1} - T_{i,j}\right) \right.
$$

$$
\left. + \frac{k_\parallel dx}{\ln\left(\frac{r_j}{r_{j-1}}\right)} \left(T_{i,j-1} - T_{i,j}\right) \right] \quad \text{(Equation 6)}
$$

where i and j represent the nodal location, M is the mass of PCM in each node, T is the nodal temperature, $k_\perp$ and $k_\parallel$ are the thermal conductivities in the axial and radial directions, respectively, r is the radius at the center location of each node, dx is the length of the nodes in the axial direction, and dr is the length of the nodes in the radial direction. In this analysis, we assumed that the PCM is static, and that conduction is the only heat transfer mechanism in the composite. Although there are density differences and some fluid motion in the composite, we expected that the fin structures will limit the impact of natural convection in the PCM bulk.

In the results shown in this paper, the properties of the PCM are set to PureTemp 4, with a transition temperature of 5°C, latent heat of 187 kJ/kg, thermal conductivity of 0.15 W/mK, average density of 880 kg/m³, and liquid and solid specific heats of 2.26 and 1.78 kJ/kgK, respectively. The PCM was placed in an aluminum fin structure. We assumed aluminum thermal conductivity of 236 W/mK, density of 2,662 kg/m³, and a specific heat of 0.91 kJ/kgK, and that the fin geometry is identical to the experiment. In this model, the heat transport through the PCM and fins was lumped using effective medium theory. The effective properties were calculated using Equations 7, 8, 9, 10, and 11 below, where the PCM and fin subscripts denote the thermophysical properties of PureTemp 4 and aluminum, respectively, the eff subscript denotes the lumped properties of the composite, and φ_{PCM} is the volume fraction of PCM.

$$
k_\parallel = \varphi_{PCM} k_{PCM} + (1 - \varphi_{PCM}) k_{fin} \quad \text{(Equation 7)}
$$

$$
k_\perp = \left(\frac{\varphi_{PCM}}{k_{PCM}} + \frac{1 - \varphi_{PCM}}{k_{fin}} \right)^{-1} \quad \text{(Equation 8)}
$$

$$
\rho_{eff} = \varphi_{PCM} \rho_{PCM} + (1 - \varphi_{PCM}) \rho_{fin} \quad \text{(Equation 9)}
$$

$$
c_{eff} = \varphi_{PCM} \frac{\rho_{PCM}}{\rho_{eff}} c_{PCM} + (1 - \varphi_{PCM}) \frac{\rho_{fin}}{\rho_{eff}} c_{fin} \quad \text{(Equation 10)}
$$

$$
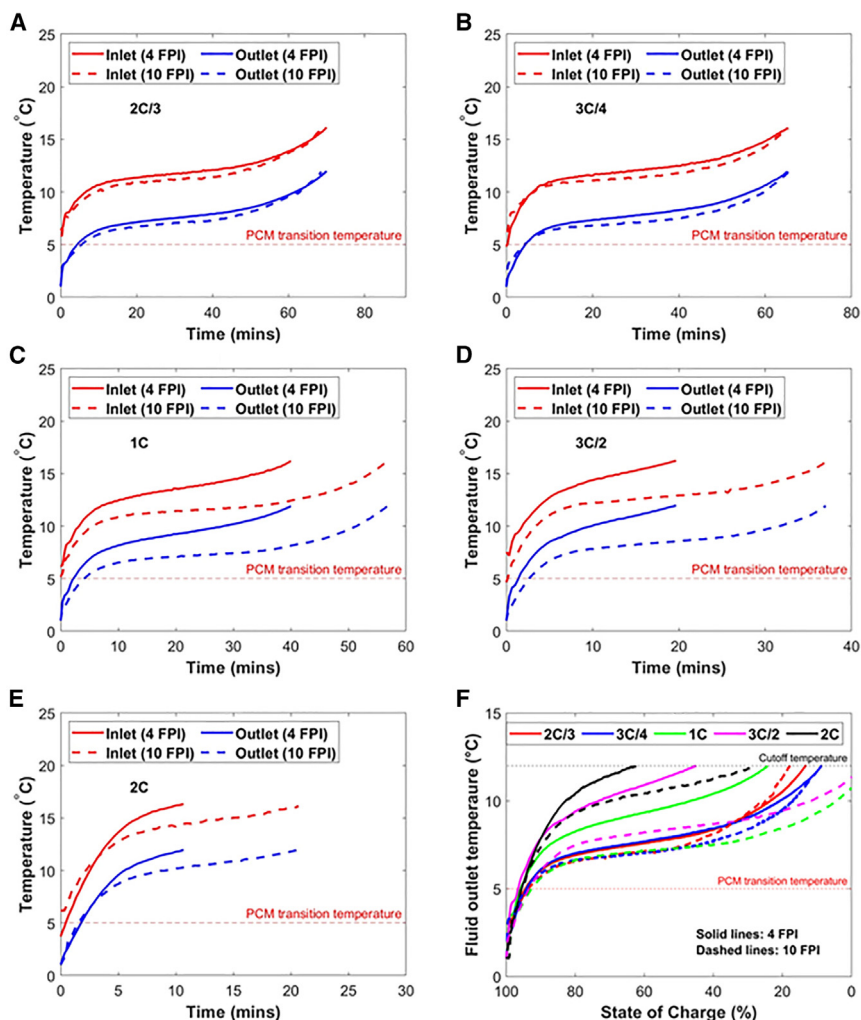L_{eff} = \varphi_{PCM} \frac{\rho_{PCM}}{\rho_{eff}} L_{PCM} \quad \text{(Equation 11)}
$$

Figure 4. Inlet and outlet fluid temperature at various desired C rates
(A) 2C/3, (B) 3C/4, (C) 1C, (D) 3C/2, (E) 2C, (F) rate capability plots for each C rate. All plots terminate at the fluid outlet cutoff temperature of 12°C, resulting in lower measured discharge time than the expected value.

The PCM enthalpy and fluid temperature are numerically integrated to calculate the thermodynamic properties in the next timestep using the Euler approach. Finally, the PCM phase and temperature are calculated using the enthalpy-temperature relations derived using the effective composite properties shown above.

Discharge time and rate capability plots

Figure 4 shows the rate capability plots for the 4 and 10 FPI TES under different desired C rates. C rate, as defined, is the inverse of time (in hours) required to charge or discharge an energy storage system; therefore, it can be noted that the discharge time decreases as the C rate increases. Higher C rate also results in higher fluid flow rate, and thus the higher heat transfer rate from the TES to the propylene glycol-water mixture. For each C rate, heat is added to the TES until the fluid outlet temperature reaches the cutoff temperature, set at 12°C in this study. For standard space conditioning applications, the air temperature leaving the cooling coil is typically maintained at around 13°C/55°F; therefore, the cutoff temperature of 12°C for fluid outlet of the TES was selected. As shown in Table 2, the measured discharge time for

Table 2. Desired versus measured discharge time for different C rates for 4 and 10 FPI TES at 12°C fluid outlet cutoff temperature

Desired C rates	Desired discharge time (min)	Measured discharge time at cutoff temperature (min)	
		4 FPI	10 FPI
2C/3	90	70.1	68.9
3C/4	80	65.3	65.6
1C	60	40.3	57.0
3C/2	40	19.8	37.2
2C	30	10.9	20.7

all the cases is lower than the target value because the fluid outlet exceeds the cutoff before the PCM is fully melted. The closer the measured discharge time to the desired discharge time, the higher is the discharge capacity of the TES. A large difference between the measured and the desired discharge time indicates a large portion of the PCM remained solid before the fluid outlet temperature reaches the cutoff temperature, thus lower discharge capacity.

In terms of discharge time, the 10 FPI and 4 FPI TES performed nearly identically when the desired C rate was below 3C/4; however, the former out-performs the latter when the desired C rate is greater than 3C/4. This can be explained because the TES thermal conductance becomes increasingly important at high C rate (>3C/4), leading to better performance by the 10 FPI device. The consequences of this observation can be seen more clearly in the power and capacity plots described in the next section.

Figure 4F summarizes the rate capability plots for all the cases. The rate capability plot is important because it shows the state-of-charge (SOC) of the TES as the fluid outlet temperature progresses to the cutoff value. If the TES is appropriately designed, the fluid outlet temperature at the desired C rate remains below the cutoff when TES reaches SOC of 0%. This indicates that the entire energy stored in the TES is adequately utilized for the intended application. On the other hand, if the TES has poor thermal conductance or the C rate is higher than the designed value, fluid outlet temperature reaches the cutoff value prematurely at SOC > 0%, indicating only partial utilization of TES storage capacity. At all the C rates, the fluid outlet temperature of the 4 FPI TES is higher than that of the 10 FPI TES. In addition, the fluid outlet temperature for the 4 FPI TES reaches the cutoff sooner than the 10 FPI TES. In other words, the 4 FPI TES utilizes the PCM less effectively due to its higher thermal resistance. Consequently, the 4 FPI TES is expected to deliver a lower discharge capacity than the 10 FPI TES, as we will discuss in subsequent sections.

Discharge power and capacity plots
Figure 5 shows the discharge power and capacity versus time under different desired C rate conditions. Note all plots end when the fluid outlet temperature reaches 12°C cutoff threshold. It is expected that the discharge power will increase with an increase in the desired C rate due to the higher heat transfer rate between the PCM and the thermal fluid. On the other hand, the discharge capacity decreases with an increase in the desired C rate because of the limitations related to heat diffusion within the PCM that cause the outlet fluid temperature to prematurely reach the cutoff temperature.

The 10 FPI TES accesses more of the PCM's stored cooling than the 4 FPI TES, providing a higher discharge capacity (Figures 5A—5E). The impact of higher effective thermal conductivity is less evident when the C rate is small (<3C/4), but it
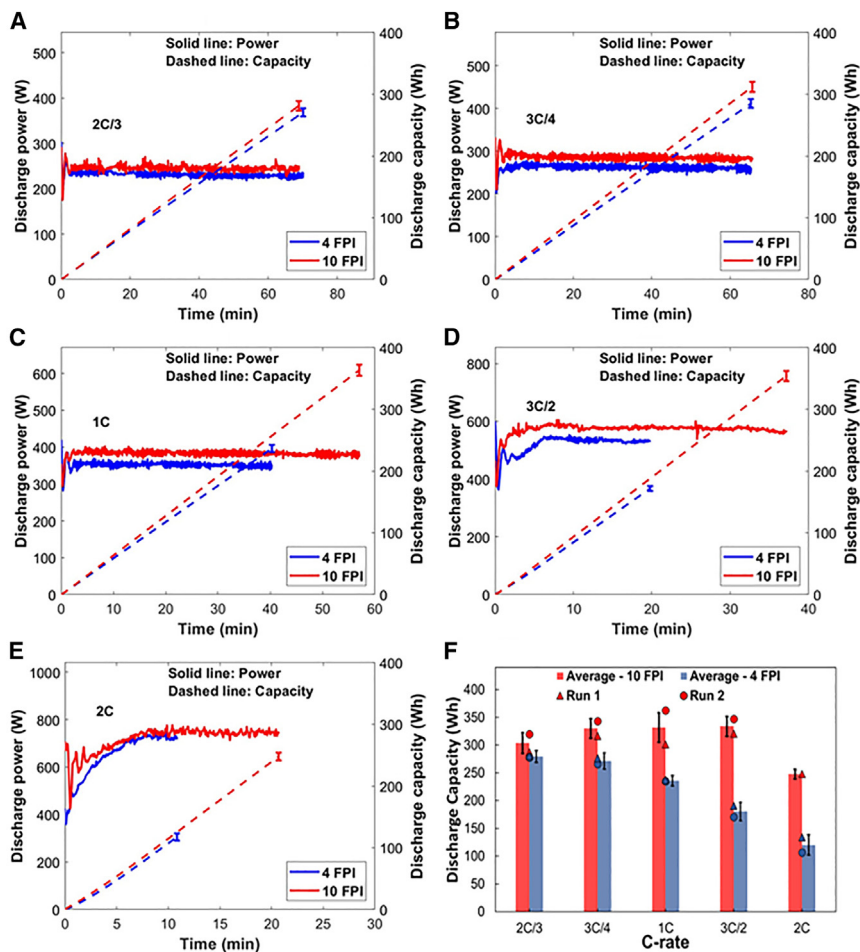
Figure 5. Discharge power and capacity plots at various desired C rates

(A) 2C/3, (B) 3C/4, (C) 1C, (D) 3C/2, (E) 2C, (F) net discharge capacity for each C rate. All plots terminate at the fluid outlet cutoff temperature of 12°C. Error bars represent uncertainty calculated using the root-sum-of-squares method and the measurement uncertainty of each sensor in the experimental setups.

becomes increasingly significant as the C rate increases above 1C. Also, note that the discharge power for the 10 FPI TES is slightly higher than that of the 4 FPI TES at the same desired C rates. This is because of the higher storage capacity of the 10 FPI TES than the 4 FPI TES, as indicated in Table 1.

Figure 5F summaries the discharge capacity for all the cases. In the case of 10 FPI TES, the available discharge capacity was fully delivered at all the C rates, except 2C, before the fluid outlet temperature reached the cutoff value of 12°C. In the case of 4 FPI TES, however, the discharge capacity significantly reduced with an increase in the C rate beyond 3C/4. The maximum reduction in discharge capacity at a 12°C cutoff temperature was observed at a C rate of 2C for both TES devices. However, the reduction in the discharge capacity was only 33.5% for the 10 FPI TES in comparison with 62.5% for the 4 FPI TES. This indicates that the higher fin density significantly affects the TES discharge capacity at the higher rate of discharging, and its effect decreases as the discharge is reduced. This observation is consistent with the results reported in prior publications in the literature. For instance, a numerical analysis on longitudinal fins by Yang et al.[47] reported that the heat transfer area is a major factor in enhancing
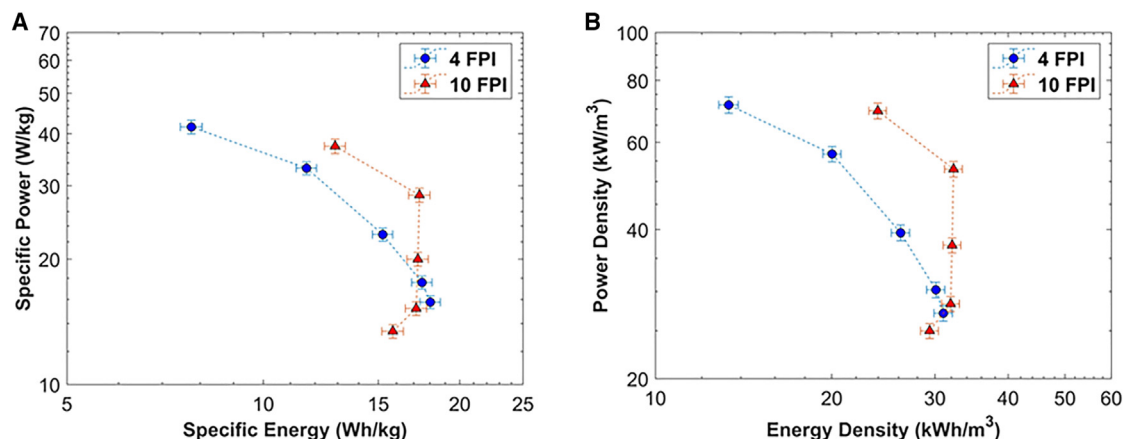
Figure 6. Ragone plots

(A) Specific power versus specific energy and (B) volumetric power density versus volumetric energy density for 4 and 10 FPI TES at different C rates for cutoff temperature of 12°C. A base-10 log scale is used for the axes. Error bars represent uncertainty calculated using the root-sum-of-squares method and the measurement uncertainty of each sensor in the experimental setups.

the effective utilization of the thermal energy storage available in the finned-tube heat exchanger. In addition, while the fin thickness is the same for both the 4 FPI and 10 FPI TES, the volume fraction of metal is much higher in the case of 10 FPI TES (20%) than 4 FPI TES (8%). The higher volume fraction of metal results in nearly two and half times higher effective thermal conductivity than that of 4 FPI finned tube. The high effective thermal conductivity as well as higher effective surface area for nearly the same total TES capacity enhances the discharge capacity at high C rate (>1C).

We also observed a slight reduction in the TES discharge capacity in the 10 FPI TES when the desired C rate was small (<3C/4), but a clear peak was only evident in one of the experimental runs (10 FPI run 2 in Figure 5F). Repeated data showed a nearly constant discharge capacity for all C rates below 3C/2, as expected. Although the discharge capacity could drop for long discharge times due to thermal gains from the ambient, we did not see strong evidence that thermal gains would have a strong impact on the performance when approximate interactions with the environment were included in our model. The reason for variability in the experimental results between the two runs, particularly for 10 FPI, is unknown.

Specific energy, energy density, and Ragone plots

Figure 6 depicts the Ragone plot for the 4 FPI and 10 FPI TES devices, with specific power on the y axis and specific energy on the x axis. Specific energy and specific power signify the total stored energy and the rate at which the energy is stored or delivered per unit mass of the TES system, respectively. Similarly, volumetric energy density and volumetric power density signify the total stored energy and the rate at which the energy is stored or delivered per unit volume of the TES system, respectively. Specific energy (SE), specific power (SP), volumetric energy density (ED), and volumetric power density (PD) values are calculated based on the expressions shown below.

SE

$$SE = \frac{\int_o^\tau \dot{m}_f c_{p,f} \left| T_{f,out} - T_{f,in} \right| dt}{M_{TES}} \qquad \text{(Equation 12)}$$

SP

$$SP = \frac{\frac{1}{\tau}\int_{o}^{\tau} \dot{m}_f c_{p,f} \left| T_{f,out} - T_{f,in} \right| dt}{M_{TES}}$$

(Equation 13)

Volumetric ED

$$ED = \frac{\int_{o}^{\tau} \dot{m}_f c_{p,f} \left| T_{f,out} - T_{f,in} \right| dt}{V_{TES}}$$

(Equation 14)

Volumetric PD

$$PD = \frac{\frac{1}{\tau}\int_{o}^{\tau} \dot{m}_f c_{p,f} \left| T_{f,out} - T_{f,in} \right| dt}{V_{TES}}$$

(Equation 15)

where τ denotes the time until the given cutoff temperature is reached. The TES mass (M_{TES}) includes the metal fins and tubes, PCM, and PVC shell. All other components such as inner rods, insulations, connecting tubing, etc., are ignored. The TES volume (V_{TES}) represents the total volume of the device without insulation or connecting tubing.

The specific power and power density for the 4 FPI device is higher than that for the 10 FPI device at any given C rate due to lower mass of the 4 FPI TES (15.5 kg) compared with the 10 FPI TES (19.1 kg). The difference in the mass of the two devices is mainly due to the higher metal fraction in the 10 FPI case. The mass of the PCM in both devices is nearly the same (~5.73 kg for 4 FPI and ~5.80 kg for 10 FPI). As shown in Figure 6, the specific energy, is higher for the 10 FPI TES than the 4 FPI TES at higher C rates (>3C/4), but smaller at lower C rates (<3C/4). The volumetric energy density follows the same trends, where the tipping point between the two devices is at 2C/3. The Ragone plots are slightly deformed, compared with an ideal curve, at lower C rates. This may be the result of thermal gains from the environment, or simply variability in repeated experiments.

Phase change in the finned-tube TES

Figure 7 illustrates the PCM discharging process in the 4 FPI and 10 FPI finned-tube TES. Although the PCM melts from the center (near the copper tube), the liquid phase moves upward due to its lower density than the solid phase and remains at the top (near the outer radius of the PVC tube). The liquid phase grows as the discharge continues and the PCM fully melts.

We can also notice some air bubbles in the PCM, which are more clearly visible in the 10 FPI device. This is due to the volume/density change between solid and liquid phase of the PCM. As the discharge process continues, trapped air bubbles move upwards and coalesce to form large bubbles. We have intentionally provided a vent in the shell to allow air movement and to account for the phase change-related volume changes. This reduces the risk of leakage and structural damage to the shell due to the pressure build-up during phase change.
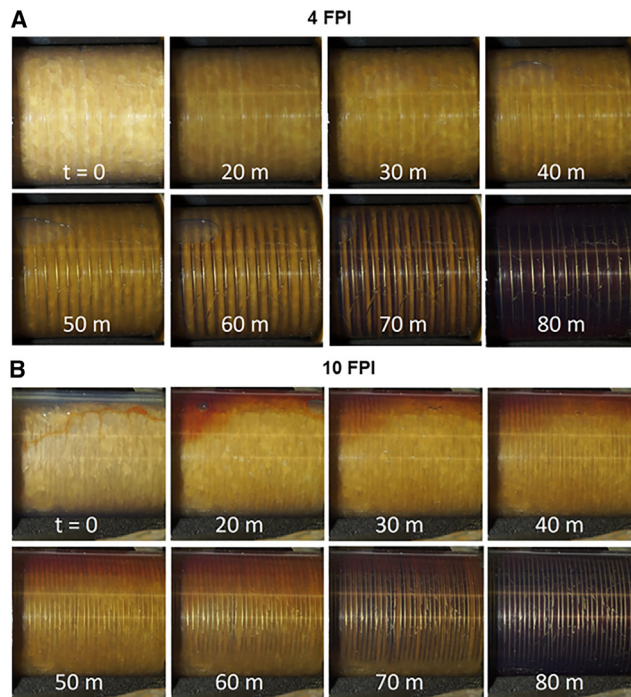
Figure 7. TES discharging process
(A) 4 FPI TES and (B)10 FPI TES at the desired C rate of 3C/4.

Finally, there are some interesting differences between the melting process for different fin pitches. These images suggest that the 10 FPI case may be melting primarily in the radial direction (away from the internal tubes), whereas in the 4 FPI case the PCM melts away from the fin surfaces in the axial direction. This indicates that the 10 FPI case may act more like an effective medium, which is discussed in more detail in the next section. These findings are in-line with past work, where the PCM primarily melts in the direction perpendicular to heat flow when the fin spacing is small, but as the fin spacing increases the PCM starts to melt away from the fins.[45]

Predictive capabilities of simplified modeling methods

One of the goals of this work was to assess if the simplified model could accurately capture the performance of finned-tube TES. Although other modeling approaches like computational fluid dynamics simulations can capture the physics driving heat transfer in fin-PCM composites, these models are intractable in optimization and system-level simulations. The proposed model is computationally inexpensive but makes two major assumptions—first that the PCM is static, and all heat transport is governed by conduction, and second that the properties of the composite PCM can be approximated using effective medium theory (Equations 7, 8, 9, 10, and 11).

The accuracy of the PCM heat exchanger model was evaluated using the experimental data shown in Figure 8, which compares the experimental results (solid lines) to the model-predicted outlet temperatures (dashed lines) when the experimental inlet temperature and flow rate were used as boundary conditions. Although the model predicts experimental trends, there are some discrepancies in the magnitude of the outlet temperature and the usable capacity.
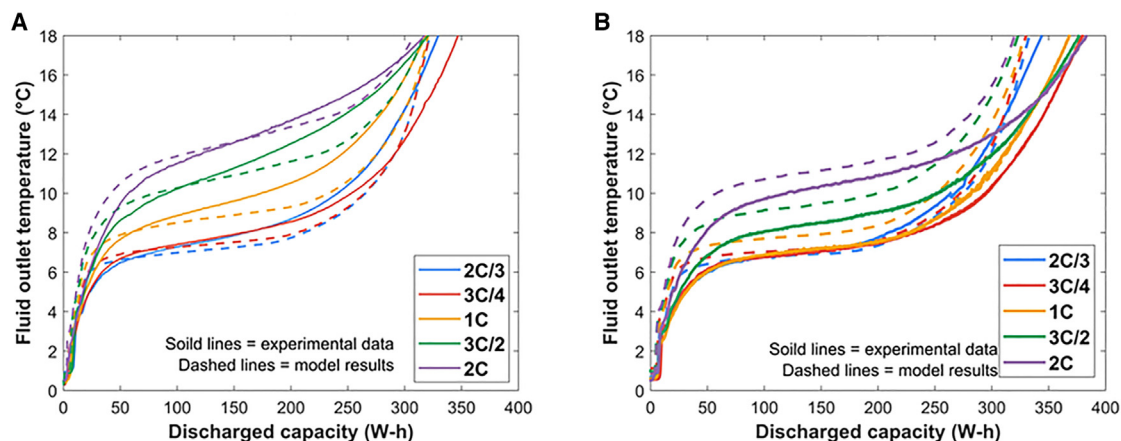
Figure 8. Comparison between experiment and model
Discharge data under different desired C rate conditions and the performance of the (A) 4 FPI TES and (B) 10 FPI TES.

Both the experimental and computational results show the expected trends seen in similar PCM heat exchangers.[30,48] The PCM starts in the fully frozen state. In the first phase of the discharge process, the glycol sensibly heats the PCM, resulting in a rapid increase in the fluid temperature to maintain the desired C rate. The predicted slope of this temperature increase versus discharged capacity during this initial increase is higher than the experiments, which is likely the result of additional thermal mass in the experiment that was not accounted for in the model (connecting tubes, u-bends, etc.).

After the initial increase, the PCM starts to change phase and the fluid outlet temperature stabilizes (second phase). As the device continues to discharge in this second phase, the fluid temperature slowly increases as a liquid layer of PCM develops between the fluid channels and the transitioning phase, resulting in an increasing thermal resistance. The impact of this internal resistances is more pronounced at higher powers (C rates) because the temperature difference between the fluid and transition temperature is directly proportional to the heat transfer rate. The thermal resistance of the liquid layer is a function of the metal volume fraction as the effective thermal conductivity will increase as the fin spacing decreases. Both the model and experiments show a decrease in the effective thermal resistance with more fins (i.e., a slower fluid temperature increase during discharge). Although this expected trend holds, the magnitude of the slope during the second phase of melting is underpredicted by the 4 FPI model. This discrepancy suggests that the effective medium assumptions may not be fully capturing the properties of the PCM composite when the fin spacing is too large. This is also evident in Figure 7, which shows that the PCM melts axially away from the fins instead of radially from the copper tube outward, as would be expected with effective properties. Previous studies have suggested that effective medium theory is only valid for small fin pitches (<2 mm), and that the apparent conductivity of a material would be lower for cases that do not fall in this bound.[45] For the 10 FPI test section, which has a fin pitch of 2.54 mm, the slope of the second discharge phase is well predicted by the model; however, there is an offset in the fluid outlet temperature. Since the offset is consistent throughout the second discharge phase for most cases, this is likely a result in an overprediction of the convective resistance in the model.[49]

Once a significant portion of the PCM has melted, the device enters the third phase of the discharge process. In this phase, some regions of the heat exchanger contain

fully liquid PCM, which reduces the effective area available for heat transfer between the fluid and transitioning PCM.[30] This effect further increases the thermal resistance within the PCM composite and results in a sharp increase in fluid temperature to maintain the desired C rate. The increase in temperature starts slowly but approaches a similar rate to the first phase of discharge once all the PCM has melted. For the 4 FPI TES (Figure 8A), the model and experiment show a similar trend, where both enter the third phase of melting after discharging about 250 Wh of cooling to the glycol. However, the 10 FPI test section enters the third phase later than predicted by the model (between 250 and 300 Wh).

Directly comparing the 4 and 10 FPI TES raises some interesting questions about the effective capacity of each device. The model just considers the PCM in the core of the heat exchanger, defined as the region with both PCM and fins. However, the test section contains a small gap between the OD of the fins (5.72 cm) and the ID of the containment vessel (6.27 cm). If the entire 10 FPI device was filled with liquid PCM (ignoring the end caps), the heat exchanger would hold 4.86 kg of PCM in the finned region and 1.55 kg in the unfinned region adjacent to the walls of the containment vessel. In the experiments, the 10 FPI TES contained 5.80 kg of PCM ($\sim$20% higher than what was expected in the core alone), suggesting that at least a portion of the unfinned volume contained PCM. In our model, the unfinned region was ignored because it has a high resistance to heat transfer due to the low intrinsic thermal conductivity of the PCM. Effectively, the model assumes that the extra cooling capacity in this region of the device is inaccessible. Although this assumption seems to hold for the 4 FPI heat exchanger, a portion of the capacity in the unfinned region seems to participate in the 10 FPI device. This may be the result of how the PCM melts in the two test sections.

When the effective thermal conductivity is high (10 FPI), the PCM will easily melt in the radial direction. When heat can pass through the liquid layer with little resistance, most of the heat will be added to the PCM near the fluid inlet and the phase front will move axially down the length of the tube once the inlet region fully melts.[48] When this occurs, regions of the PCM near the heat exchanger inlet will superheat and be held at an elevated temperature for a significant portion of the discharge process. Although the pure PCM at the periphery of the fins has a low thermal conductivity, it can melt with a high driving temperature difference over enough time. If this pure PCM melts before the outlet temperature reaches the cutoff, the capacity would become active.

At lower effective thermal conductivities (4 FPI), we expect that a smaller fraction of the heat exchanger length to be adjacent to a fully melted region of the phase change composite at a given state of charge.[48] In this case, the PCM adjacent to the low thermal conductivity region will not provide the driving temperature difference needed to melt this extra capacity, at least during most of the discharge process. Although the capacity difference is an interesting feature of this experiment, full devices will likely not have this low thermal conductivity region as many tubes with interconnected fins will be placed in parallel to reach the desired capacity.

DISCUSSION

In summary, this paper details the numerical and experimental investigation of two finned-tube-integrated TES systems, which are more deployable, scalable, and cost-effective than other TES designs that rely on expensive filler materials. The proposed TES system includes 4 and 10 FPI aluminum fins and PureTemp 4 PCM, which has a transition temperature of 5°C and latent heat of 187 kJ/kg.

The key findings of the study are summarized below.

- The charge and discharge capacities of the TES are not identical during the experiments. This is related to different thermal losses from the TES to the ambient surroundings. A simple technique comprising steady-state heat flow to estimate the effective thermal resistance between TES and ambient is described in this paper.
- The rate capability plots for the 4 and 10 FPI TES devices were nearly identical when the desired C rate was below 3C/4; however, the 10 FPI TES out-performs the 4 FPI TES when the desired C rate is greater than 3C/4 because the greater number of fins reduces the thermal resistance of the PCM composite.
- The 10 FPI TES consistently provides more cooling capacity than the 4 FPI TES and the difference becomes increasingly significant as the desired C rate increases. For the 10 FPI TES, the available discharge capacity is fully delivered at all the desired C rates, except 2C before the fluid outlet temperature reached the cutoff value of 12°C. However, in the case of the 4 FPI TES, the available discharge capacity is only fully delivered when the C rate is less than 3C/4.
- In the Ragone plot that comprises specific discharge power and specific discharge energy, the thermal benefits of 10 FPI TES becomes less prominent due to the increased mass of the fins.
- The numerical model, which assumes that conduction is the only heat transfer mechanism in the PCM composite and that the composite properties can be estimated using effective medium theory, correctly predicts the trends in the discharge performance but misses some important characteristics. Therefore, we recommend that more work is needed to develop appropriate models for the composite structures that balance computational time and accuracy.

This study is limited to TES modeling, design, experimentation, and characterization. The future steps include refining the finned-tube-PCM numerical model, scaling-up the design for practical deployment, and integration of the TES with the building HVAC systems. The thermal energy storage related benefits are expected to vary based on the building types, HVAC applications, and climatic conditions. A follow-up analysis detailing the TES impact under various operating conditions would also be beneficial for the building research community.

EXPERIMENTAL PROCEDURES

Resource availability

Lead contact
Further information and requests for resources should be directed to and will be fulfilled by the lead contact, Ravi A. Kishore (ravi.kishore@nrel.gov).

Materials availability
This study did not generate any new materials.

Data and code availability
The published article includes all data generated and analyzed during this study.

TES fabrication
The TES system consists of four shell-and-tube heat exchangers comprising polyvinyl chloride (PVC) pipes, with an ID of 2.469 in (6.271 cm) and OD of 2.875 in (7.303 cm), and copper tubes, having ID of 0.9 in (2.286 cm) and OD of 1.0 in (2.540 cm). The PVC pipe contains the PCM, while heat transfer fluid flows through

the copper tubes. A polypropylene rod, with an OD of 0.50 in (1.270 cm), was also inserted inside each of the copper tubes to increase the fluid velocity, and therefore the heat transfer coefficient. Different tubes were connected to each other using a soft PVC plastic tubing with an ID of 1.0 in (2.540 cm) and OD of 1.5 in (3.810 cm). Two different fin densities, 4 and 10 FPI, were chosen for experimental characterization and model validation. PureTemp 4 PCM was filled in the space between the outer shell and in the finned tubes. The PCM has a melting point of 5°C and latent heat storage capacity of 187 kJ kg^{-1}. Propylene glycol-water mixture (25% v/v) was using as the heat transfer fluid. All the TES tubes were insulated with a 0.5 in (1.270 cm) thick fiberglass insulation jacket encapsulated in kraft paper.

Experimentation

The test rig used for the experimentation includes a chiller (PolyScience DuraChill CA10A3T1-41AA1N), a variable-speed diaphragm pump (Pentair SHURflo 8000-543-236), and a heater (Watlow FLUENT In-line 1-kW) with a feedback loop to manage the set-point temperature. There are three thermocouples each at the inlet and outlet of the TES, a flowmeter with a feedback loop to manage the preset flowrate, and a few quarter-turn flow valves to select the appropriate flow path for charge mode (freeze PCM using the chiller) and discharge mode (melt PCM using the heater or chiller).

AUTHOR CONTRIBUTIONS

R.A.K. and A.M. designed and fabricated the device. R.A.K., A.M., and A.S. carried out the experiments. R.A.K. and A.S. conducted the data analysis and result compilations. A.M. performed the modeling. J.W. supervised the research and contributed to the analysis and discussions. All authors contributed to the writing and revision of the manuscript.

DECLARATION OF INTERESTS

The authors declare no competing interests.

REFERENCES

1. Tian, Y., and Zhao, C. (2013). A review of solar collectors and thermal energy storage in solar thermal applications. Appl. Energy *104*, 538–553.

2. Kuravi, S., Trahan, J., Goswami, D.Y., Rahman, M.M., Stefanakos, E.K., and Science, C. (2013). Thermal energy storage technologies and systems for concentrating solar power plants. Prog. Energy Combust. Sci. *39*, 285–319.

3. Weng, Y.-C., Cho, H.-P., Chang, C.-C., and Chen, S.-L.J.A.E. (2011). Heat Pipe with PCM for Electronic Cooling, *88*, pp. 1825–1833.

4. Kandasamy, R., Wang, X.-Q., and Mujumdar, A.S.J.A.T.E. (2007). Application of Phase Change Materials in Thermal Management of Electronics, *27*, pp. 2822–2832.

5. Cabeza, L.F., Castell, A., Barreneche, C., De Gracia, A., Fernández, A., and Reviews, S.E.

(2011). Materials used as PCM in thermal energy storage in buildings: a review. Renew. Sustain. Energy Rev. *15*, 1675–1695.

6. Zhou, D., Zhao, C.-Y., and Tian, Y. (2012). Review on thermal energy storage with phase change materials (PCMs) in building applications. Appl. Energy *92*, 593–605.

7. Kuznik, F., David, D., Johannes, K., Roux, J.J., and Reviews, S.E. (2011). A review on phase change materials integrated in building walls. Renew. Sustain. Energy Rev. *15*, 379–391.

8. Sharma, A., Tyagi, V.V., Chen, C., Buddhi, D., and reviews, S.e. (2009). Review on thermal energy storage with phase change materials and applications. Renew. Sustain. Energy Rev. *13*, 318–345.

9. Zhang, Y., Zhou, G., Lin, K., Zhang, Q., Di, H., and environment. (2007). Application of latent heat thermal energy storage in buildings: State-of-the-art and outlook. Build. Environ. *42*, 2197–2209.

10. Pielichowska, K., and Pielichowski, K. (2014). Phase change materials for thermal energy storage. Prog. Mater. Sci. *65*, 67–123.

11. Zalba, B., Marın, J.M., Cabeza, L.F., and Mehling, H. (2003). Review on thermal energy storage with phase change: materials. Appl. Therm. Eng. *23*, 251–283.

12. Farid, M.M., Khudhair, A.M., Razack, S.A.K., Al-Hallaj, S.J.E.c., and management. (2004). A Review on Phase Change Energy Storage: Materials and Applications, *45*, pp. 1597–1615.

13. Palacios, A., Barreneche, C., Navarro, M.E., and Ding, Y. (2020). Thermal energy storage technologies for concentrated solar power–A review from a materials perspective. Renew. Energy *156*, 1244–1265.

14. Wu, M.Q., Wu, S., Cai, Y.F., Wang, R.Z., and Li, T.X. (2021). Form-stable phase change composites: Preparation, performance, and applications for thermal energy conversion, storage and management. Energy Storage Mater. *42*, 380–417.

15. Nie, B., Palacios, A., Zou, B., Liu, J., Zhang, T., and Li, Y. (2020). Review on phase change materials for cold thermal energy storage applications. Renew. Sustain. Energy Rev. *134*, 110340.

16. Ali, H.M. (2019). Applications of combined/hybrid use of heat pipe and phase change materials in energy storage and cooling systems: A recent review. J. Energy Storage *26*, 100986.

17. Faraj, K., Khaled, M., Faraj, J., Hachem, F., and Castelain, C. (2021). A review on phase change materials for thermal energy storage in buildings: Heating and hybrid applications. J. Energy Storage *33*, 101913.

18. Triscari, G., Santovito, M., Bressan, M., and Papurello, D. (2021). Experimental and model validation of a phase change material heat exchanger integrated into a real building. Int. J. Energy Res. *45*, 18222–18236.

19. Kishore, R.A., Bianchi, M.V., Booten, C., Vidal, J., and Jackson, R. (2020). Optimizing PCM-integrated walls for potential energy savings in US Buildings. Energy Build. *226*, 110355.

20. Kishore, R.A., Bianchi, M.V., Booten, C., Vidal, J., and Jackson, R. (2021). Enhancing building energy performance by effectively using phase change material and dynamic insulation in walls. Appl. Energy *283*, 116306.

21. Moreno, P., Castell, A., Solé, C., Zsembinszki, G., and Cabeza, L.F. (2014). PCM thermal energy storage tanks in heat pump system for space cooling. Energy Build. *82*, 399–405.

22. Kishore, R.A., Bianchi, M.V., Booten, C., Vidal, J., and Jackson, R. (2021). Parametric and sensitivity analysis of a PCM-integrated wall for optimal thermal load modulation in lightweight buildings. Appl. Therm. Eng. *187*, 116568.

23. Miao, R., Kishore, R., Kaur, S., Prasher, R., and Dames, C. (2022). A non-volatile thermal switch for building energy savings. Cell Reports Physical Science *3*, 100960.

24. Wijesuriya, S., Kishore, R.A., Bianchi, M.V., and Booten, C. (2022). Potential energy savings benefits and limitations of radiative cooling coatings for US residential buildings. J. Clean. Prod. *379*, 134763.

25. Global Alliance for, B., Construction, I.E.A., and the United Nations Environment, P (2019). 2019 global status report for buildings and construction: towards a zero-emission, efficient and resilient buildings and construction sector. United Nations Environment Programme Nairobi, Kenya.

26. Kalnæs, S.E., and Jelle, B.P. (2015). Phase change materials and products for building applications: A state-of-the-art review and future research opportunities. Energy Build. *94*, 150–176.

27. Baetens, R., Jelle, B.P., and Gustavsen, A. (2010). Phase change materials for building applications: A state-of-the-art review. Energy Build. *42*, 1361–1368.

28. Sharma, A., Chauhan, R., Ali Kallioğlu, M., Chinnasamy, V., and Singh, T. (2021). A review of phase change materials (PCMs) for thermal storage in solar air heating systems. Mater. Today: Proc. *44*, 4357–4363.

29. Liu, Y., Zheng, R., and Li, J. (2022). High latent heat phase change materials (PCMs) with low melting temperature for thermal management and storage of electronic devices and power batteries: Critical review. Renew. Sustain. Energy Rev. *168*, 112783.

30. Woods, J., Mahvi, A., Goyal, A., Kozubal, E., Odukomaiya, A., and Jackson, R. (2021). Rate capability and Ragone plots for phase change thermal energy storage. Nat. Energy *6*, 295–302.

31. Yazdani, M.R., Laitinen, A., Helaakoski, V., Farnas, L.K., Kukko, K., Saari, K., and Vuorinen, V. (2021). Efficient storage and recovery of waste heat by phase change material embedded within additively manufactured grid heat exchangers. Int. J. Heat Mass Tran. *181*, 121846.

32. Cao, M., Huang, J., and Liu, Z. (2020). The enhanced performance of phase-change materials via 3D printing with prickly aluminum honeycomb for thermal management of ternary lithium batteries. Adv. Mater. Sci. Eng. *2020*, 1–11.

33. Qureshi, Z.A., Al Omari, S.A.B., Elnajjar, E., Mahmoud, F., Al-Ketan, O., and Al-Rub, R.A. (2021). Thermal characterization of 3D-Printed lattices based on triply periodic minimal surfaces embedded with organic phase change material. Case Stud. Therm. Eng. *27*, 101315.

34. Li, H., Tay, R.Y., Tsang, S.H., Hubert, R., Coquet, P., Merlet, T., Foncin, J., Yu, J.J., and Teo, E.H.T. (2022). Thermally conductive and leakage-proof phase-change materials composed of dense graphene foam and paraffin for thermal management. ACS Appl. Nano Mater. *5*, 8362–8370.

35. Wu, S., Li, T.X., Yan, T., Dai, Y.J., and Wang, R.Z. (2016). High performance form-stable expanded graphite/stearic acid composite phase change material for modular thermal energy storage. Int. J. Heat Mass Tran. *102*, 733–744.

36. Agyenim, F., Eames, P., and Smyth, M. (2009). A comparison of heat transfer enhancement in a medium temperature thermal energy storage heat exchanger using fins. Sol. Energy *83*, 1509–1520.

37. Agyenim, F., Hewitt, N., Eames, P., and Smyth, M. (2010). A review of materials, heat transfer and phase change problem formulation for latent heat thermal energy storage systems (LHTESS). Renew. Sustain. Energy Rev. *14*, 615–628.

38. Deng, S., Nie, C., Jiang, H., and Ye, W.-B. (2019). Evaluation and optimization of thermal performance for a finned double tube latent heat thermal energy storage. Int. J. Heat Mass Tran. *130*, 532–544.

39. Zhang, C., Li, J., and Chen, Y. (2020). Improving the energy discharging performance of a latent heat storage (LHS) unit using fractal-tree-shaped fins. Appl. Energy *259*, 114102.

40. Yang, J. (2022). Experimental Investigation of a Phase Change Material Charged Finned-Tube Heat Exchanger. Purdue University. https://docs.lib.purdue.edu/cgi/viewcontent.cgi?article=3429&context=iracc.

41. Gil, A., Peiró, G., Oró, E., and Cabeza, L.F. (2018). Experimental analysis of the effective thermal conductivity enhancement of PCM using finned tubes in high temperature bulk tanks. Appl. Therm. Eng. *142*, 736–744.

42. Rahimi, M., Ranjbar, A.A., Ganji, D.D., Sedighi, K., and Hosseini, M.J. (2014). Experimental investigation of phase change inside a finned-tube heat exchanger. J. Eng. *2014*, 1–11.

43. Zayed, M.E., Zhao, J., Li, W., Elsheikh, A.H., Elbanna, A.M., Jing, L., and Geweda, A.E. (2020). Recent progress in phase change materials storage containers: Geometries, design considerations and heat transfer improvement methods. J. Energy Storage *30*, 101341.

44. Esen, M., Durmuş, A., and Durmuş, A. (1998). Geometric design of solar-aided latent heat store depending on various parameters and phase change materials. Sol. Energy *62*, 19–28.

45. Tamraparni, A., Hoe, A., Deckard, M., Zhang, C., Elwany, A., Shamberger, P.J., and Felts, J.R. (2021). Design and optimization of lamellar phase change composites for thermal energy storage. Adv. Eng. Mater. *23*, 2001052.

46. Rohsenow, W.M., Hartnett, J.P., and Cho, Y.I. (1998). Handbook of Heat Transfer (Mcgraw-hill).

47. Yang, X., Wang, X., Liu, Z., Luo, X., and Yan, J. (2022). Effect of fin number on the melting phase change in a horizontal finned shell-and-tube thermal energy storage unit. Sol. Energy Mater. Sol. Cell. *236*, 111527.

48. Huang, R., Mahvi, A., Odukomaiya, W., Goyal, A., and Woods, J. (2022). Reduced-order modeling method for phase-change thermal energy storage heat exchangers. Energy Convers. Manag. *263*, 115692.

49. Mahvi, A., Shete, K.P., Odukomaiya, A., and Woods, J. (2022). Measuring the maximum capacity and thermal resistances in phase-change thermal storage devices. J. Energy Storage *55*, 105514.